

RESEARCH ARTICLE

Clinical Translation of Tumor Acidosis Measurements with AcidoCEST MRI

Kyle M. Jones,¹ Edward A. Randtke,² Eriko S. Yoshimaru,³ Christine M. Howison,² Pavani Chalasani,⁴ Robert R. Klein,⁵ Setsuko K. Chambers,^{3,6} Phillip H. Kuo,^{1,2,3} Mark D. Pagel^{1,2,3}

¹Biomedical Engineering Graduate Interdisciplinary Program, University of Arizona, Tucson, AZ, USA

²Department of Medical Imaging, University of Arizona, 1515 N. Campbell Ave., Tucson, AZ, 85724-5024, USA

³University of Arizona Cancer Center, Tucson, AZ, USA

⁴Division of Hematology-Oncology, University of Arizona, Tucson, AZ, USA

⁵Department of Pathology, University of Arizona, Tucson, AZ, USA

⁶Department of Obstetrics and Gynecology, University of Arizona, Tucson, AZ, USA

Abstract

Purpose: We optimized acido-chemical exchange saturation transfer (acidoCEST) magnetic resonance imaging (MRI), a method that measures extracellular pH (pHe), and translated this method to the radiology clinic to evaluate tumor acidosis.

Procedures: A CEST-FISP MRI protocol was used to image a flank SKOV3 tumor model. Bloch fitting modified to include the direct estimation of pH was developed to generate parametric maps of tumor pHe in the SKOV3 tumor model, a patient with high-grade invasive ductal carcinoma, and a patient with metastatic ovarian cancer. The acidoCEST MRI results of the patient with metastatic ovarian cancer were compared with DCE MRI and histopathology.

Results: The pHe maps of a flank model showed pHe measurements between 6.4 and 7.4, which matched with the expected tumor pHe range from past acidoCEST MRI studies in flank tumors. In the patient with metastatic ovarian cancer, the average pHe value of three adjacent tumors was 6.58, and the most reliable pHe measurements were obtained from the right posterior tumor, which favorably compared with DCE MRI and histopathological results. The average pHe of the kidney showed an average pHe of 6.73 units. The patient with high-grade invasive ductal carcinoma failed to accumulate sufficient agent to generate pHe measurements.

Conclusions: Optimized acidoCEST MRI generated pHe measurements in a flank tumor model and could be translated to the clinic to assess a patient with metastatic ovarian cancer.

Key Words: CEST MRI, pH, Bloch fitting, Respiration gating, Cancer

Electronic supplementary material The online version of this article (doi:10.1007/s11307-016-1029-7) contains supplementary material, which is available to authorized users.

Correspondence to: Mark Pagel; e-mail: mpagel@u.arizona.edu

Introduction

Tumor metabolism often relies on aerobic glycolysis to produce energy and molecular building blocks that are required for biosynthesis in rapidly proliferating cells,

known as the Warburg effect [1]. An increased glycolysis leads to increased production of lactic acid, which causes the extracellular pH (pHe) to become lower in the tumor microenvironment [2]. Aggressive tumors are often more metabolically active, and therefore, the tumor pHe may be used to evaluate tumor aggressiveness [3, 4]. Furthermore, treatments that inhibit tumor metabolism can often slow the rate of glycolysis, leading to reduced lactic acid production in the tumor microenvironment. Thus, an increased tumor pHe may indicate an early response to therapy [5].

We have measured pHe in tumor models of human cancers with chemical exchange saturation transfer (CEST) magnetic resonance imaging (MRI) [6–9]. Our specific “acidoCEST MRI” protocol measures the two CEST signals produced by the amide protons of iopamidol (Isovue™, Bracco Imaging, Inc.), which is FDA-approved for clinical CT studies that we have repurposed for CEST MRI exams [10]. These CEST signals are linearly correlated with pH because the exchange of amide protons and water protons is base-catalyzed [11].

In this study, we aimed to optimize the acidoCEST MRI acquisition protocol for clinical translation. In particular, we sought to improve our analysis methods to avoid overfitting noisy CEST spectra, especially when CEST signal amplitudes are low [12]. This problem is exacerbated at lower magnetic field strengths due to greater overlap of features in a CEST spectrum. We investigated fitting CEST spectra with the Bloch equations modified for chemical exchange (described as Bloch fitting for the remainder of this report) [13]. We also incorporated the measurement of pH directly into this Bloch fitting method to improve the determination of pH values. Finally, we investigated the clinical translation of improved acidoCEST methods to the radiology clinic, to evaluate a patient with high-grade invasive ductal carcinoma and a patient with metastatic epithelial ovarian cancer.

Material and Methods

Simulations

CEST spectra were constructed using the Bloch equations and the experimentally determined exchange rates of iopamidol. To simulate an *in vivo* difference CEST spectrum at a particular pH value and B_0 field strength, pre-injection and post-injection spectra were simulated by setting the concentration of iopamidol to 0 and 20 mM, respectively. White Gaussian noise was added to each pre-injection and post-injection CEST spectrum at a signal-to-noise ratio (SNR) of 40 and then the post-injection spectrum was subtracted from the pre-injection spectrum. An SNR of 40 and a concentration of 20 mM were chosen because the simulated difference CEST spectrum was similar to *in vivo* CEST spectra from our past studies [14]. Bloch fitting was performed on the simulated difference CEST spectrum to estimate the pH value. This spectrum was also fit with three Lorentzian line shapes to account for the CEST signals from the two amide protons and the hydroxyl groups of iopamidol using our previously reported fitting method [15]. This process was repeated 100 times with different white

Gaussian noise for each repetition. These simulations were performed at 7 T magnetic field strengths with 3.5 μ T saturation power and at 3 T field strength with 3.5 and 1.5 μ T saturation powers, which matched the B_0 and B_1 combinations that were used for *in vivo* studies.

MRI Studies of Chemical Solutions

The 600 MHz NMR, 7 T MRI, and 3 T MRI studies were performed with chemical solutions and acquisition methods (Table S1) as described in the Electronic Supplementary Material. Each solution was tested in a 600 MHz Bruker NMR spectrometer at 37.0 ± 0.5 °C by applying a B_0 gradient along the solution’s long axis to perform ultrafast CEST MRI [16]. These results were acquired from -7.5 to 0 ppm, -2.5 to 5 ppm, and 2.5 to 10 ppm to compensate for diffusion that would affect results generated from testing the full range of -7.5 to 10 ppm. The region used for Bloch fitting of the CEST spectra used a region of -5 to 10 ppm. The B_0 gradient was adjusted relative to in-plane spatial resolution to generate a CEST spectrum with 0.03 ppm increments. The base-catalyzed exchange rate (k_b) and uncatalyzed exchange rate (k_o) of each exchanging pool of iopamidol were determined by fitting the Bloch equations to the CEST spectra of solutions at different pH values (Eq. 1). The acid-catalyzed exchange rate (k_a) was assumed to be negligible for all exchanging pools.

$$k_{\text{ex}} = k_o + k_b 10^{(\text{pH}-\text{pKw})} \quad (1)$$

This analysis allowed us to incorporate the pH into the Bloch equations as a fitting parameter, along with the concentration of the agent, T_1 and T_2 relaxation time constants of water, B_0 value, and two scale factors to account for potential changes in the baseline of the CEST spectrum.

In Vivo MRI Acquisition Methods

MRI of the Flank Tumor Model The preparation of the mouse model for MRI studies is described in the Electronic Supporting Material. We performed a multi-slice, spin echo MRI acquisition to localize the flank tumor and measure tumor volume (Table S1). We then performed four pre-injection acidoCEST MRI scans to obtain a spectrum of endogenous CEST signals. Each acidoCEST MRI scan consisted of 40 saturation frequencies that were acquired in 3:47 min. After injecting 3.7 mg/ml iopamidol, an infusion pump was connected to the catheter line to deliver the agent at 400 μ l/h throughout the remainder of the scan session. Six post-injection acidoCEST MRI scans were then obtained. The total scan time was 37:50 min.

Delayed Gadolinium Enhancement Imaging of a Patient with Metastatic Ovarian Cancer A multi-slice gradient echo MRI protocol was used 2 weeks prior to CEST MRI to collect MR images that were enhanced by an intravenous injection of 8 ml of 529 mg/ml gadobenate dimeglumine (MultiHance®, Bracco Imaging, Inc., Princeton, NJ). Images were acquired prior to injection, 30 s after injection (arterial-enhanced image), 60 s after injection (venous-enhanced image), and 4 min after injection (delayed enhanced image).

CEST MRI of Patients with High-Grade Invasive Ductal Carcinoma and Metastatic Ovarian Cancer At the start of clinical acidoCEST MRI, a multi-slice, gradient echo MRI protocol without respiration gating was used to localize the tumor. A WASSR MRI protocol identified the B_0 offset. The saturation period consisted of ten rectangular pulses each with a 99 ms duration and a 0.1 ms delay. This sequence was repeated from -2 to 2 ppm in 0.1 ppm increments to generate a water line profile in a total time of 36 s.

We used an ungated acidoCEST MRI pulse sequence for patient imaging, which used a saturation period composed of 20 rectangular pulses, each 99 ms long followed by a 1 ms delay (Fig. S1). After each saturation period, a turboFLASH sequence was used to acquire an MR image that was identical to that used with the WASSR MRI protocol. This sequence was repeated with a series of 20 saturation frequencies at 3.0 to 6.9 ppm in 0.1 ppm increments, referenced to the water frequency set to 0 ppm as determined from WASSR MRI results. After the last of 10 pre-injection scans, we delivered iopamidol (370 mg/ml) at 1 ml/s for 60 s and then at 0.2 ml/s for 5 min via a catheter inserted in the arm, for a total of 120 ml of injection volume. Fifteen post-injection scans were acquired immediately after the first 60 s of injection. The total scan time for the pre-injection and post-injection scans was 23:45 min.

Image Analysis

Details of the Bloch fitting and Lorentzian line shape fitting (a.k.a. Lorentzian fitting) methods are provided in the Electronic Supplementary Material. To measure the tumor volume in each mouse, the areas of image regions representing tumor tissue were manually selected and summed using ImageJ.

pH Analysis of the Chemical Solutions Four MR images were acquired and averaged. A CEST spectrum was constructed for each pixel within a region of the image that contained the chemical solutions as well as intermediate space filled with agar or water. These spectra represented post-injection spectra because the chemical solutions contained iopamidol. To generate a pre-injection spectrum for each pixel, a one pool Lorentzian line shape for the water peak was fit to the spectrum. The experimental spectrum was then subtracted from this fitted Lorentzian line shape to generate a difference CEST spectrum. Bloch fitting and Lorentzian fitting were performed on this difference CEST spectrum.

pHe Analysis of the Flank Tumor Model For the flank tumor model, the average of the four pre-injection MR images and the average of the six post-injection MR images were each spatially smoothed with Gaussian filtering, for each set of images acquired at a specific saturation frequency (Fig. S1). The resulting pre-injection image was subtracted from the post-injection image acquired at each saturation frequency. A CEST spectrum was constructed for each pixel from these difference images. Each difference CEST spectrum was fit with Lorentzian line shapes and Bloch fitting.

The median value from the pixelwise pHe values of the tumor represented the total tumor pHe. In the pixelwise parametric maps, we limited the minimum pHe to 6.2 and the maximum pHe to 7.4

because results with chemical solutions showed that Bloch fitting was reliable between those values. Additionally, pHe values above 7.4 are unlikely in tumors because tumor pHe is not expected to be alkaline.

pHe Analysis of Patients The Bloch and Lorentzian fitting analyses of the imaging results from both patients were identical to the fitting process for the flank tumor model because pre-injection and post-injection images were acquired while the agent was administered intravenously. As an exception, we changed the saturation pulse power and time used for the Bloch fitting procedure to match the conditions of the saturation period of our clinical imaging protocol. The first five repetitions of the post-injection scans of the patient with metastatic ovarian cancer had CEST contrast greater than $2 \cdot \sqrt{2} \cdot \text{noise}$, which was approximately 2 %. Contrast greater than this threshold has a 95 % probability of arising from the agent [2]. The remaining 10 repetitions had CEST contrast less than $2 \cdot \sqrt{2} \cdot \text{noise}$ so those repetitions were discarded from data analysis and we only averaged the first five repetitions of the post-injection scans for our average post-injection image.

For the patient with high-grade invasive ductal carcinoma, all repetitions of the post-injection scans appeared to have little to no agent uptake. Therefore, we averaged all of the post-injection scans for our average post-injection image. All ten of the pre-injection scans were averaged for the pre-injection average image for the two patients. All subsequent analysis was identical to analysis of the flank tumor model. Finally, for the parametric maps, pixels with evidence for contrast agent uptake and with pHe values above 7.0 were set to 7.0 and pixels below 6.2 were set to 6.2 because the pHe values were only reliable between these values at 3 T magnetic field strength based on our experiments with chemical solutions.

Histological Analysis

Tumor tissues from the patient with metastatic ovarian cancer were removed during surgery, prepared for histopathology, and stained with standard Hematoxylin & Eosin (H&E).

Results

Simulations

Our simulations showed that Bloch fitting generated accurate pH values from pH 6.2 to 7.4 at 7 and 3 T magnetic field strengths (Fig. 1a, b, d, e). Lorentzian fitting underestimated pH values from pH 6.4 to 7.4 with a more severe underestimation at higher pH values at 7 T. Bloch fitting provided precise pH measurements from pH 6.4 to 7.4 at 7 T. The precision of pH estimates with Bloch fitting at 3 T was moderate throughout the pH range and less precise than pH estimates at 7 T. Lorentzian fitting provided precise pH measurements from pH 6.2 to 6.8 at 7 T but were much less precise at higher pH values. Lorentzian fitting at 3 T was imprecise, especially at higher pH values (Fig. 1b). The better performance of Bloch fitting compared to Lorentzian fitting showed that Bloch fitting can fit spectra

when 1 peak is small or nonexistent, which is apparent below pH 6.2 and above pH 7.0 at 7 T and below pH 6.4 and above pH 6.8 at 3 T. The better performance of Bloch fitting and Lorentzian fitting at 7 T compared to 3 T is due to better peak separation at 7 T.

Bloch fitting produced more accurate pH estimates with a 1.5 μ T saturation pulse than a 3.5 μ T saturation pulse at 3 T (Fig. 1c, f). The improved accuracy was attributed to better peak separation with a lower saturation pulse power. However, a low saturation pulse power necessitates a higher concentration of agent delivery to generate CEST effects that can be distinguished from the noise in a CEST spectrum. We used the lower saturation power for subsequent studies because accurate pH estimates at 3 T were more important than estimating inaccurate pH measurements in cases where agent delivery was low.

Experimental Studies with Chemical Solutions

Our experimental studies showed that Bloch fitting generated more accurate pH measurements with chemical solutions below pH 6.4 and above pH 7.0 compared to Lorentzian fitting at 7 T (Fig. 2b, c). These results matched well with simulation results and demonstrate that the dynamic range for pH measurements with Bloch fitting is greater than with Lorentzian fitting. Lorentzian fitting was unable to generate accurate pH measurements of chemical solutions at 3 T whereas Bloch fitting was able to generate accurate and precise pH measurements at pH 6.4 to 7.0 (Fig. 2e, f). This experimental result demonstrated that acidoCEST MRI is feasible at 3 T with Bloch fitting,

although the dynamic range is smaller than at 7 T. Additionally, Bloch fitting at both 3 and 7 T estimated pH values above 7.4 in areas where the chemical solutions were nonexistent, which can be easily filtered and removed from the pH parametric map. Lorentzian fitting often estimated pH values in areas without chemical solutions, demonstrating that Lorentzian fitting is more susceptible to overfitting into the noise of a CEST spectrum.

Evaluations of the AcidoCEST MRI Protocol for the Tumor Model

All ten mice of the flank tumor model survived throughout the study (Table S2). Some pHe measurements were not determined from some MRI scan sessions due to insufficient uptake of the agent resulting in a 40 % success rate (16/40) in measuring tumor pHe in the flank model. This success rate indicated that the need for high agent uptake in tumor tissues is a potential pitfall of the acidoCEST MRI technique.

We applied Bloch fitting to analyze each CEST spectrum from each pixel within the tumor area. Our Bloch fitting method was less sensitive to noise and therefore was not susceptible to overfitting (Fig. S2a). For comparison, Lorentzian fitting methods were sensitive to noise and caused overfitting of the CEST spectrum (Fig. S2b). Additionally, Bloch fitting used seven parameters (pHe, concentration, T_1 relaxation time constant of water, T_2 relaxation time constant of water, B_0 offset, and two scale factors to account for the baseline changing between the pre-injection and post-injection scans), which are fewer than the

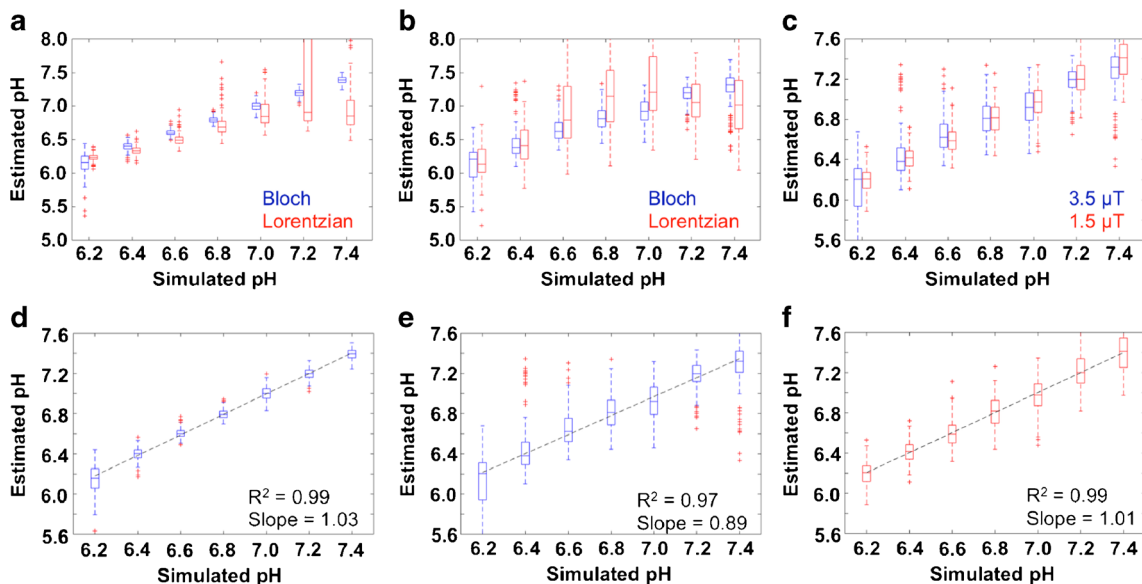


Fig. 1. Simulation results. Box plots were created from the fitted pH values of the 100 simulated difference CEST spectra for **a** Lorentzian fitting and Bloch fitting at 7 T, **b** Lorentzian fitting and Bloch fitting at 3 T with a 3.5 μ T saturation pulse, and **c** Bloch fitting at 3 T with a 3.5 μ T saturation pulse and Bloch fitting at 3 T with a 1.5 μ T saturation pulse. The best fit line was generated from the median values of the box plots for **d** Bloch fitting at 7 T, **e** Bloch fitting at 3 T with a 3.5 μ T saturation pulse, and **f** Bloch fitting at 3 T with a 1.5 μ T saturation pulse.

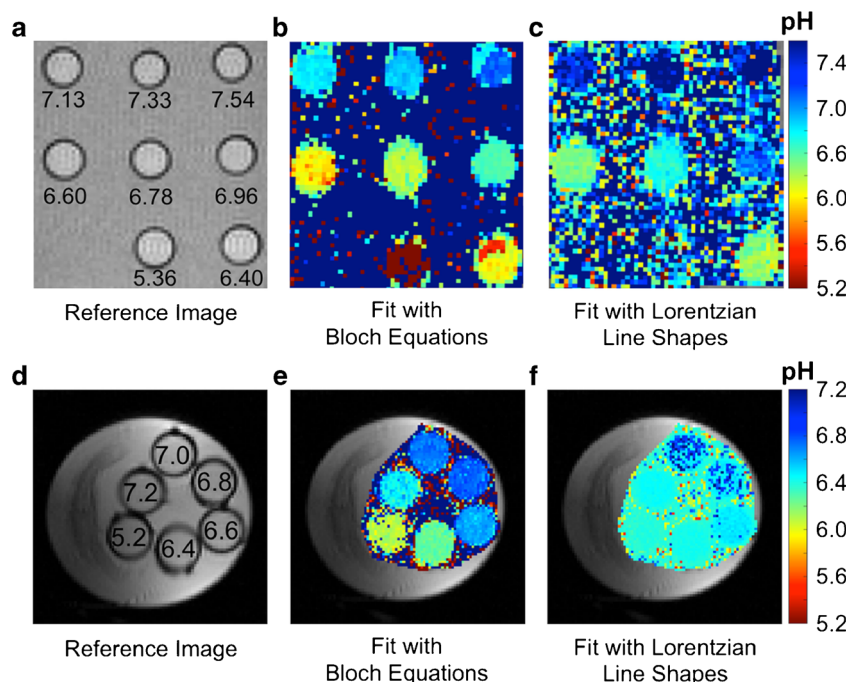


Fig. 2. AcidoCEST MRI results with chemical solutions at 7 T and 3 T. **a** A reference image at 7 T shows the location of each sample, labeled with the pH value. pH measurements using **b** Bloch fitting and **c** Lorentzian fitting at 7 T show that pH estimates are more accurate and precise with Bloch fitting. **d–f** A similar set of images and parametric maps were obtained at 3 T.

nine parameters required for Lorentzian fitting (amplitude, width and center frequency for three Lorentzian line shapes). Fitting fewer parameters may provide a more robust estimate of pHe.

The Bloch fitting analysis estimated a concentration of 5 to 100 mM in the flank tumor following injection and infusion (Fig. 3b). This concentration generated exogenous CEST signals that were larger than endogenous CEST signal amplitudes. To ensure that our analyses were unaffected by endogenous CEST signals, we assumed that the endogenous contrast was static throughout the imaging session, and we subtracted the averaged, smoothed pre-injection image from the averaged, smoothed post-injection image at each saturation frequency (Fig. S1).

Evaluations of AcidoCEST MRI Results for the Tumor Model

A representative pHe map of a flank tumor generated with Bloch fitting (Fig. 3a) showed pHe measurements between 6.4 and 7.4 throughout the tumor. This pHe range matches well with the expected tumor pHe range from past acidoCEST MRI studies, indicating that Bloch fitting generated reasonable pHe measurements. In contrast, a representative pHe map of a flank tumor fit with Lorentzian line shapes showed some pHe measurements below 6.4 and above 7.4 (Fig. 3c). This result indicated that fitting with Lorentzian line shapes is more susceptible to generating unreasonable pHe measurements.

Flank tumor volumes were 50–150 mm³ for the first MRI scan and 350–550 mm³ for the final MRI scan. Larger tumor volumes were correlated with a more acidic pHe in the flank tumor model, indicating that this tumor model became more metabolically active during tumor growth (Fig. 3d). The parametric maps showed a larger pHe range within the tumor with Lorentzian fitting than with Bloch fitting, which was attributed to the lower precision offered by Lorentzian fitting (Fig. 3e). Both tumor models fit with Bloch and Lorentzian fitting showed no relationship between tumor volume and concentration of agent in the tumor, suggesting that each tumor model had consistent vascular flow and permeability characteristics during tumor growth.

A comparison between Bloch and Lorentzian fitting of the median values of the pixelwise maps for each mouse imaged showed a weak but positive correlation indicating that pHe measurements were similar between the two fitting methods (Fig. 3f). However, Lorentzian fitting is susceptible to overestimating the pHe quite dramatically at pHe values greater than 7.0 (Fig. 3g).

Evaluations of the AcidoCEST MRI Protocol for Patients

Clinical acidoCEST MRI was performed with a 50-year-old patient who presented with a grade I invasive ductal carcinoma in the left breast. The 7.4 × 3.4 × 5.5 cm irregular enhancing, hypermetabolic multicentric mass in the lateral aspect was confirmed to be ER+/PR+/HER– following

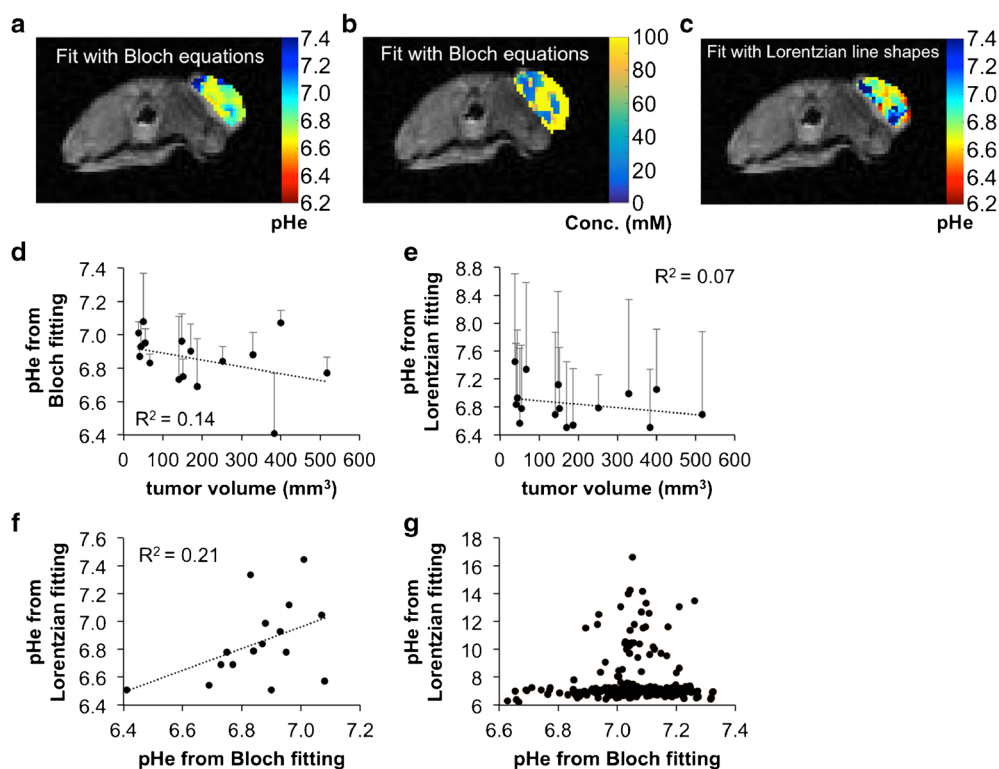


Fig. 3. AcidoCEST MRI of the flank tumor model. **a** A representative parametric map of tumor pHe and of **b** concentration determined with Bloch fitting of the flank tumor model is overlaid on the anatomical image. **c** A parametric map of tumor pHe determined with Lorentzian fitting of the flank tumor model is overlaid on the anatomical image. **d** The flank tumor model showed a weak inverse correlation between pHe and tumor volume when analyzed with Bloch fitting, suggesting increased metabolism as the tumor grew larger. **e** This correlation was weaker when the pixels were analyzed with Lorentzian fitting. *Error bars* represent the standard deviation of the pixelwise map for a particular mouse. **f** When comparing the median values from the parametric pHe maps analyzed with Bloch fitting and Lorentzian fitting on a mouse by mouse basis, there was a weak positive correlation, suggesting that results from the two fitting methods were similar but not identical. **g** Within the same mouse, pixel values from Bloch and Lorentzian fitting were more similar when Bloch fitting estimated low pHe values compared to when Bloch fitting estimated high pHe values.

biopsy. The same imaging protocol was performed with a 69-year-old patient who presented with a high-grade serous carcinoma. The 8.8-cm perigastric mass was 2-deoxy-2- ^{18}F fluoro-D-glucose avid, was confirmed to be ER+/Pax-8+ following biopsy, and was presumed to be a metastasis from a prior malignant tumor of the ovary.

Both patients reported no discomfort with i.v. injection and the MRI scan session, which supported the clinical feasibility of this method. Slight patient movement was evident in the anatomical MR images of the patient with metastatic ovarian cancer. However, the movement did not cause motion artifacts in the FISP images. The Gaussian spatial filter used for each FISP image corrected for the slight changes in location of the tissues for this patient. The tumors were easily identified with the T_1 -weighted gradient echo sequence.

The rapid wash out of iopamidol from the tumors did not provide sufficient time to acquire a full CEST spectrum with good CNR. Therefore, we acquired 15 post-injection images with saturation offsets between 3.0 and 6.9 ppm. We adjusted the saturation offsets to match this range by

determining the water MR frequency from the WASSR MRI results. We used a range that was larger than 4.2 to 5.6 ppm to accommodate B_0 inhomogeneity, which was estimated to be 0.2 ppm within the tumor.

Evaluations of AcidoCEST MRI Results for Patients

Because both patients were imaged with a 3 T MRI scanner, the two peaks of the agent were overlapped in the CEST spectra for most pixels in the image of the tumors (Fig. S2c and S2d). Yet the acidoCEST MRI acquisition and analysis method still produced a parametric map of the pHe of the tumors. The patient with high-grade invasive ductal carcinoma produced unreliable pHe measurements with Bloch and Lorentzian fitting, which was attributed to low uptake of the agent (Fig. 4). The patient with metastatic ovarian cancer showed higher uptake of the agent in the tumors, allowing for reliable pHe measurements in the tumors and the kidney with Bloch fitting (Fig. 5). Lorentzian fitting showed pHe

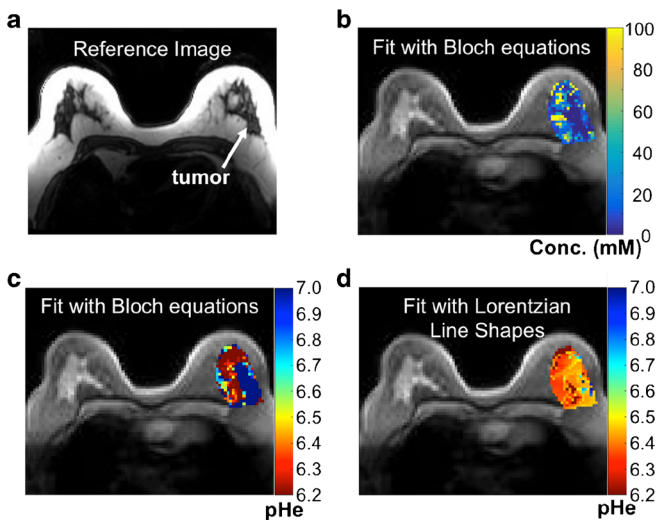


Fig. 4. Parametric maps of the patient with high-grade invasive ductal carcinoma. **a** A representative image of the patient with high-grade invasive ductal carcinoma. **b** A parametric map of tumor pHe determined with Bloch fitting is overlaid on the anatomical image. **c** A parametric map of tumor concentration determined with Bloch fitting is overlaid on the anatomical image. **d** A parametric map of tumor pHe determined with Lorentzian fitting is overlaid on the anatomical image.

measurements of approximately 6.4 throughout the tumors and kidney, which further demonstrates that Lorentzian fitting is unable to measure pHe at 3 T. Our parametric maps for both Bloch and Lorentzian fitting consisted of pHe values only between pHe 6.2 and 7.0 with pHe values above 7.0 set to our maximum threshold of 7.0, because results with chemical solutions showed that Bloch fitting at 3 T was unreliable outside of this range. Analysis of the pHe map generated from Bloch fitting showed that the right posterior tumor provided the most reliable pHe measurements. The average pHe value of this right posterior tumor was 6.79 units, and the standard deviation of the pHe values throughout this tumor was 0.21 units.

In the patient with metastatic ovarian cancer, the agent accumulated with an 84 mM concentration in the right posterior tumor, 56 mM in the left posterior tumor, and 58 mM in the anterior tumor. However, the estimation of concentration is highly correlated with T_1 . For instance, it was apparent during the fitting process that the concentration estimates were sometimes overestimated due to an underestimation of T_1 . Thus, in future studies, concentration estimates could be improved by acquiring a T_1 map. The DCE MRI evaluation of the tumor demonstrated good delayed enhancement of the right posterior tumor (Fig. 5d–g), consistent with a tumor that was both vascular and fibrous. The other two tumors did not show the same delayed enhancement from DCE MRI, suggesting that the agent would have lower uptake in these tumors. Thus, the concentration of agent determined via acidoCEST MRI compared favorably

with the DCE MRI results. DCE MRI may be useful for pre-screening patients who have tumors that can be analyzed with acidoCEST MRI.

The three tumors of the patient with metastatic ovarian cancer were classified with histology (Fig. S3). The anterior tumor was primarily composed of cells and showed little protein or vascularity. The left posterior tumor was similar to the anterior tumor and also had a fibrous capsule along the edge, which matched with the delayed enhancement DCE MR image that typically results from high accumulation of the agent in fibrous tumor regions. The right posterior tumor showed higher vascularity and more fibrous tissue than the other two tumors, which correlated with results from the delayed enhancement DCE MR image. Therefore, the histopathological results supported the observation that tumor pHe measurements were reliable in the right posterior tumor due to higher vascularity and fibrosity that facilitated higher contrast agent uptake and retention.

The parametric pHe map of the kidney of the patient with metastatic ovarian cancer generated with Bloch fitting showed an average pHe of 6.73 units, with a standard deviation of 0.24 units (Fig. 5a). The outer cortex showed reliable pHe measurements between pHe 6.2 and 7.0, but the inner medulla had pHe values below 6.2, which is below our minimum threshold for our range of reliable pHe measurements. These results matched the acidic inner medulla and more neutral outer cortex that we and others have observed in mouse tumor models, which further supported that our clinical acidoCEST MRI protocol produces reliable pHe measurements. The average concentration of the agent in the outer cortex was estimated to be 80 mM, and the concentration in the inner medulla was 69 mM, which provided assurance that sufficient agent had collected in the kidney to produce strong CEST MRI signals.

Discussion

This study has established the clinical translation of acidoCEST MRI from imaging of a flank tumor model to the clinical imaging evaluation of a patient with metastatic ovarian cancer. The comparison of pHe measurements estimated with Bloch fitting compared to Lorentzian fitting were more accurate and precise in simulations, chemical solutions, a flank tumor model, and a patient.

Iopamidol was previously used to measure pHe of the bladder in a patient, whereby the bladder accumulated high concentrations of the agent for the pHe measurement [17]. This previous report did not indicate that reliable pHe measurements were made in other organs, which may be related to the level of uptake of the agent in these other organs. Similarly, in the patient with metastatic ovarian cancer, we observed a high concentration of agent throughout the kidney and sufficient concentration in the right posterior tumor for pHe measurements, while the other two tumors had lower uptake of agent that made the pHe measurements less reliable for these tumors. In the patient

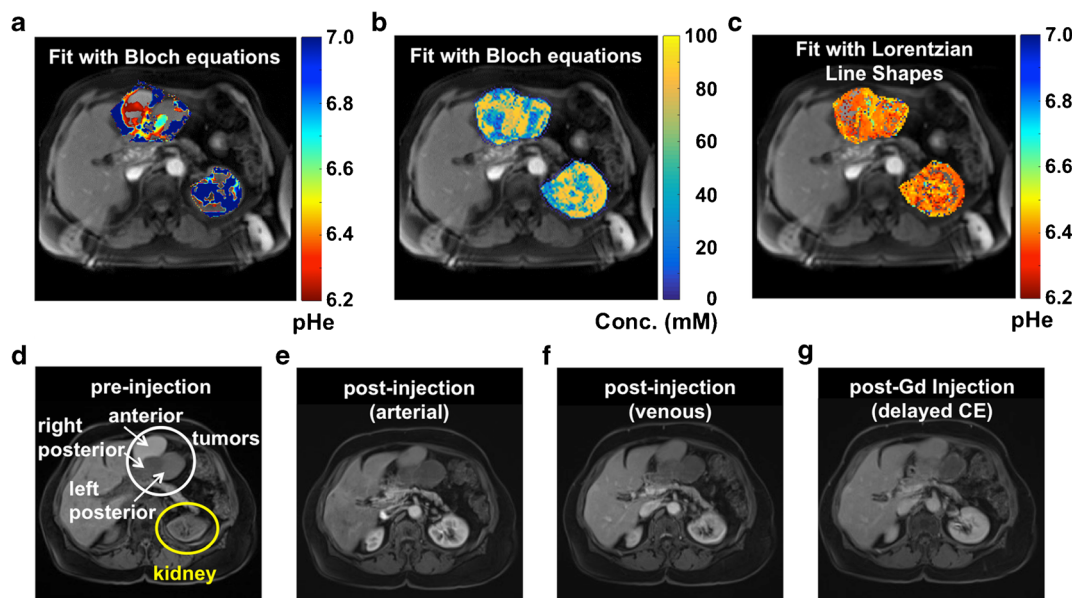


Fig. 5. Parametric maps of the patient with metastatic ovarian cancer. **a** A parametric map of tumor pHe determined with Bloch fitting is overlaid on the anatomical image. **b** A parametric map of tumor concentration determined with Bloch fitting is overlaid on the anatomical image. **c** A parametric map of tumor pHe determined with Lorentzian fitting is overlaid on the anatomical image. **d** A gradient echo MR image showed the location of the tumor and kidney. **e** Arterial, **f** venous, and **g** delayed contrast enhanced gradient echo MR images showed different levels of agent uptake in each tumor.

with high-grade invasive ductal carcinoma, low uptake of the agent was seen throughout the tumor and nearby tissue. This evidence indicates that pHe measurements can only be made in tissues with high uptake of the agent.

The previous study of bladder pHe was limited to measurements of pHe below 7.0, because the CEST signal at 5.6 ppm is weak above this pHe value, which obviates a ratiometric analysis of two CEST signals. We also observed this limitation, which prompted us to replace our previous ratiometric analysis method with a new Bloch fitting method to determine pHe. Our Bloch fitting method does not require two distinguishable CEST signals in the CEST spectrum, which allowed us to measure pHe above 7.0 at 7 T. Bloch fitting of CEST spectra is a significant technological advancement, further improving clinical translation of acidoCEST MRI.

CEST MRI has been used in the clinic to measure amide proton transfer (APT), an endogenous CEST effect that arises from chemical exchange between proteins and water [18, 19]. However, APT MRI is sensitive to the concentration of mobile proteins in tissues as well as pH, so that normal and pathological tissues with different protein concentrations may be misinterpreted as having a difference in pHe. Furthermore, APT MRI is sensitive to other conditions such as saturation power and endogenous T_1 relaxation time of the tissue. For comparison, acidoCEST MRI with an exogenous CEST agent can measure pHe in a manner that is independent of concentration, saturation power, and T_1 relaxation time, which offers advantages relative to APT MRI.

Future studies are warranted to understand the utility of this new molecular imaging method for clinical diagnoses. Future studies should investigate the relationship between *in vivo* pHe measurements and *ex vivo* analyses of pH-related molecular biomarkers, to further understand the relationship between tumor acidosis and molecular drivers in cancer. Future studies should also investigate the change in tumor pHe in early response to therapies that directly target the lactate production pathway or that indirectly affect metabolism that can cause a general reduction in lactate production. Future clinical studies may establish that measurements of tumor pHe can be used as an independent marker to improve the diagnosis and care of each individual cancer patient through personalized medicine. These many reasons justify the continued clinical translation and development of acidoCEST MRI.

Compliance with Ethical Standards

Conflict of Interest

The authors declare that they have no conflict of interest.

References

1. Warburg O (1956) On the origin of cancer cells. *Science* 123:309–314
2. Chen LQ, Pagel MD (2015) Evaluating pH in the extracellular tumor microenvironment using CEST MRI and other imaging methods. *Adv Radiol*. doi:10.1155/2015/206405

3. Gatenby RA, Gawlinski ET, Gmitro AF et al (2006) Acid mediated tumor invasion: a multidisciplinary study. *Cancer Res* 66:5216–5223
4. Estrella V, Chen T, Lloyd M (2013) Acidity generated by the tumor microenvironment drives local invasion. *Cancer Res* 73:1524–1535
5. Akhenblit PA, Pagel MD (2016) Recent advances in targeting tumor energy metabolism with tumor acidosis as a biomarker of drug efficacy. *J Cancer Sci Therapy* 8:20–29
6. Chen LQ, Howison CM, Jeffery JJ (2013) Evaluations of extracellular pH within *in vivo* tumors using acidoCEST MRI. *Magn Reson Med* 72:1408–1417
7. Sheth VR, Li Y, Chen LQ (2012) Measuring *in vivo* tumor pHe with CEST-FISP MRI. *Magn Reson Med* 67:760–768
8. Liu G, Li Y, Sheth VR, Pagel MD (2012) Imaging *in vivo* extracellular pH with a single PARACEST MRI contrast agent. *Mol Imaging* 1:47–57
9. Sheth VR, Liu G, Li Y, Pagel MD (2012) Improved pH measurements with a single PARACEST MRI contrast agent. *Contrast Media Mol Imaging* 1:26–34
10. Aime S, Calabi L, Biondi L (2005) Iopamidol: exploring the potential use of a well-established x ray contrast agent for MRI. *Magn Reson Med* 53:830–834
11. Liepinsh E, Otting G (1996) Proton exchange rates from amino acid side chains—implications for image contrast. *Magn Reson Med* 1:30–42
12. Jones KM, Randtke ER, Howison CM et al (2015) Measuring extracellular pH in a lung fibrosis model with acidoCEST MRI. *Mol Imaging and Biol* 2:177–184
13. Woessner DE, Zhang S, Merritt MEG, Sherry AD (2005) Numerical solution of the Bloch equations provides insights into the optimum design of PARACEST agents for MRI. *Magn Reson Med* 53:790–799
14. Moon BF, Jones KM, Chen LQ et al (2015) A comparison of iopromide and iopamidol, two acidoCEST MRI contrast media that measure tumor extracellular pH. *Contrast Media Mol Imaging* 10:446–455
15. Hingorani DV, Montano LA, Randtke EA et al (2015) A single diamagnetic catalyCEST MRI contrast agent that detects cathepsin B enzyme activity by using a ratio of two CEST signals. *Contrast Media Mol Imaging* 11:130–138
16. Dopfert J, Zaiss M, Witte C, Schroeder L (2014) Ultrafast CEST imaging. *J Magn Reson* 243:47–53
17. Muller-Lutz A, Khalil N, Schmitt B et al (2014) Pilot study of iopamidol-based quantitative pH imaging on a clinical 3 T MR scanner. *Magn Reson Mater Phy* 27:477–485
18. Harston GWJ, Tee YK, Blockley N et al (2015) Identifying the ischaemic penumbra using pH-weighted magnetic resonance imaging. *Brain A J Neurol* 138:36–42
19. Ma B, Blakeley JO, Hong X et al (2016) Applying amide proton transfer-weighted MRI to distinguish pseudoprogression from true progression in malignant gliomas. *J Magn Reson Imaging*. doi:10.1002/jmri.2515